

RESEARCH ARTICLE

Printed Liquid Crystal Optical Vortex Beam Generators

Mengmeng Li, Steve J. Elston, Chao He, Xuke Qiu, Alfonso A. Castrejón-Pita, and Stephen M. Morris*

This study presents an innovative application of inkjet printing technology in the construction of a switchable optical vortex beam generator. The fabrication process involves drop-on-demand printing of liquid crystal (LC) droplets that can generate an optical vortex beam in the far-field with the application of a voltage. Notably, this vortex beam can be activated and deactivated by manipulating the amplitude of the electric field. Both simulations and experiments are used to determine the optical characteristics of the printed LC devices and the resulting far-field patterns for different polarizations of light. The study showcases the versatility of the generator in that it can produce both vortex and vector beams, the choice of which is simply determined by the polarization of the input light. This highlights the potential of this printed LC technology for integration into a multitude of optical systems.

nanostructured glass plates,^[31] mode converters,^[32,33] helical mirror,^[34] dielectric wedges,^[35] and metasurfaces.^[36–38]

Liquid crystals (LCs) are a desirable media for vortex beam generation as they exhibit natural birefringence and can form complex spatial profiles of the retardance, which are needed to create complex optical phase profiles. Moreover, their internal structure (i.e., the average pointing direction of the molecules) and consequently their optical properties can be finely tuned by an applied voltage. Previous demonstrations of vortex beam generation using LCs have included the formation of inhomogeneously aligned nematic LC structures such as q-plates^[39,40] and LC droplets^[40,41] that

enable the generation of vortex beam with different topological charge. Additionally, umbilics^[40,42] formed inside LCs as well as homeotropic LC light valves^[40,43] have also been shown to form similar structures.

In terms of LC droplets, vortex beam generation has been demonstrated when such droplets are dispersed within water, forming micron-sized spherical droplets. In the presence of a surfactant (e.g., 4'-n-pentyl-4-cyanobiphenyl), the LC director in these droplets assumes a radially symmetric 3D spatial structure, centered on the droplet's core. This behavior stems from the creation of defects at the droplet's center, leading to a distribution of the LC director around the defect. Coupled with the birefringent optical properties of nematic LCs, this specific distribution gives rise to a helical wavefront and thus a vortex beam. While the fabrication method for this LC droplet-based vortex beam generator is relatively straightforward, controlling the droplet's diameter can prove to be a challenge. Tunable optical vortex beam generators based on patterned LCs have also involved the self-organization of defects that in turn give rise to vortex beam creation; although such generators typically require specific orientation of the LC director in addition to the use of patterned transparent electrodes.^[44]

In general, LC-based vortex beam generation techniques often involve rather complex device architectures and/or structuring of the LC director profile. For example, q-plate vortex beam generators utilize polarization-sensitive alignment techniques such as photoalignment layers, which can suffer from poor long-term device stability. Grating-based generators, on the other hand, typically rely on gratings that require the use of photolithography, adding complexity and cost to the fabrication process. Similarly, LC spiral plate-based generators demand advanced fabrication techniques such as direct laser writing. While being highly versatile, spatial light modulator-based vortex beam generators enable

1. Introduction

An optical vortex beam is a type of optical beam that exhibits several remarkable features including helical phase fronts, a region of zero intensity at the center of the beam, and orbital angular momentum. These unique characteristics ensure that vortex beams have the potential to play an important role in a wide gamut of applications such as optical tweezers,^[1–3] hemispherical microlasers,^[4] optical communications,^[5,6] quantum entanglement,^[7,8] nanotechnology,^[9] nonlinear optics,^[10–12] optical machining,^[13] astronomy,^[14] microscopy and imaging,^[15–17] biomedicine and chemistry,^[18,19] and metrology.^[20] These diverse applications have demanded the development of methods with which to generate vortex beams whereby the essence of generating a vortex beam is based upon changing the phase of the input light into one that represents a helical structure. This process can be realized in a number of ways including by using spiral phase plates,^[21–23] diffractive optical elements,^[24,25] computer-generated holograms,^[26–28] segmented deformable mirrors,^[29,30]

M. Li, S. J. Elston, C. He, X. Qiu, A. A. Castrejón-Pita, S. M. Morris
Department of Engineering Science
University of Oxford
Parks Road, Oxford OX1 3PJ, UK
E-mail: stephen.morris@eng.ox.ac.uk

The ORCID identification number(s) for the author(s) of this article can be found under <https://doi.org/10.1002/adom.202400450>

© 2024 The Author(s). Advanced Optical Materials published by Wiley-VCH GmbH. This is an open access article under the terms of the [Creative Commons Attribution](#) License, which permits use, distribution and reproduction in any medium, provided the original work is properly cited.

DOI: 10.1002/adom.202400450

complex optical phase profiles to be generated on-demand but at the expense of cost and size. Each technique, therefore, typically involves either intricate fabrication processes or elaborate optical systems (or in some cases both). As a result, alternative fabrication techniques that can be used to manufacture LC optical vortex beam generators on-demand and that are flexible in design would be highly desirable.

A fabrication technique that might offer a solution to this problem is micron-scale drop-on-demand printing, which has attracted tremendous attention from many different diverse fields including medical,^[45–47] electronics,^[48–51] agriculture,^[52,53] and biology^[54,55] due to its high accuracy, compatibility with a wide variety of materials and substrates, and rapid prototyping/fabrication process. It can enable the development of sophisticated 2D patterns and architectures of a range of materials without the need for photomasks. Here, we demonstrate the fabrication of a LC optical vortex beam generator that has been fabricated using inkjet printing technology and that can be activated and deactivated with the application and removal of an electric field. This approach provides a straightforward method that enables the formation of high-order vortex beam generators and/or arrays that are compact with the ability to generate either vector or vortex beams. Being able to fabricate such generators on-demand such that the beam-generation can be turned-on or off with an applied voltage potentially broadens the scope of vortex beam applications providing ease of integration into various optical systems.

2. Results and Discussion

The procedure for the construction of the vortex beam generator is illustrated in **Figure 1**. In the process developed herein, a nematic LC, specifically the mixture E7 (Synthon Chemicals), was employed. The process commences with the coating of an indium tin oxide (ITO) glass slide with a lecithin solution (1% by weight in isopropanol—see Experimental Section) which was then spin-coated at 800 rpm and left for a period of time to allow for the solvent to evaporate (Steps i to iii). The deposition of the lecithin solution was needed to ensure a homeotropic alignment of the nematic LC droplet at the LC/glass substrate. This treated substrate then served as a platform for the printing of the nematic LC droplet. The printing procedure was executed utilizing a Jetlab-II system (MicroFab Technologies Inc), equipped with a three-axis translation platform that facilitated precise positioning of the LC droplets. An integrated camera provided real-time monitoring of the droplet shape and quality. Utilizing a nozzle with an 80 μm inner diameter, the system printed LC droplets with in-flight and deposited footprint diameters measuring 70 and 95 μm , respectively. Subsequent printing at the same location resulted in a cumulative droplet footprint of 280 μm (Step iv). A second glass substrate spin-coated with a wet polyvinyl alcohol (PVA) solution (Steps v–vii) was then positioned over the printed LC droplet. The integrity of this layered assembly was ensured through the incorporation of two spacers positioned at opposing sides of the droplet and fastened securely with an adhesive. A detailed description of this fabrication protocol is provided in Experimental Section.

Figure 2 illustrates the optical characteristics of a printed LC droplet on a lecithin-coated glass substrate (**Figure 2a**) but no top

glass substrate (as indicated by step iv) in **Figure 1**) as well as that for the printed LC vortex beam generator devices without (**Figure 2b**) and with (**Figure 2c**) an applied voltage (after step vii) in **Figure 1**). For each device, the series of images in each row is as follows: the initial image (far left) shows the optical texture as observed on a polarizing optical microscope (POM) with crossed polarizers, followed by an image that depicts the optical retardance across the printed droplet/devices. The third image in the sequence represents the fast axis distribution and the sequence concludes with a schematic representation of the director distribution within the droplet/device. The changes observed in the optical properties when the droplet was assembled into a device and a voltage was applied can be attributed to changes in the distribution of the LC director within the droplet/device.

The optical properties (namely the retardance and orientation of the fast axis) were characterized using a Mueller Matrix (MM) polarimetry microscope (see Experimental Section). This specific type of polarimetry based on the determination of the MM, is capable of evaluating the anisotropic optical attributes of microstructures, including the birefringence and diattenuation.^[56] When LC droplets were deposited onto lecithin-treated ITO slides (first row of images), the LC director within the droplet generally aligned homeotropically, i.e., perpendicularly to the substrate surface and the LC/air interface. However, due to surface tension effects, the director alignment is shifted to become perpendicular to the droplet surface around its periphery. This resulted in the formation of a distinctive dark cross pattern under crossed polarizers, as depicted in **Figure 2a**. These director distribution characteristics and the inherent birefringence properties of nematic LCs cause the droplet's retardance to increase to the highest value and then decrease at the edge of the droplet along the radius from the center point to the edge.

In contrast, when another ITO-coated glass slide, coated with a PVA layer, was introduced on top of the droplet, the director orientation at the top interface is altered to align itself preferentially parallel to the surfaces thereby forming a “windmill”-like director distribution structure. The corresponding retardance, demonstrated in **Figure 2b**, exhibits marked differences compared to the pre-sandwiched LC droplet. Nevertheless, the phase shift induced by this new LC director distribution does not convert incident linearly polarized light into a vortex beam (see Supporting Information). It is only when an appropriate electric field is applied normal to the glass substrates that a vortex beam was observed in the far-field. With the application of an electric field, the LC director reorients, causing the device to function as a half-wave plate with an order number $m = 2$. This is demonstrated experimentally later in the paper.

A comparative analysis of the retardance diagrams (second column in **Figure 2**) reveals that the field-off configuration (**Figure 2b**) displays a somewhat nonuniform retardance, resulting in a broad range of values, whereas the field-on condition (**Figure 2c**) exhibits a more uniform retardance. The fast axis (third column in **Figure 2**) undergoes an annular 2π shift in the azimuthal direction in all cases. Further discussion in relation to the results from simulations of the retardance and fast axis distribution will follow shortly.

In the context of **Figure 2b**, which illustrates the sandwiched device in a state without an applied voltage, there are points

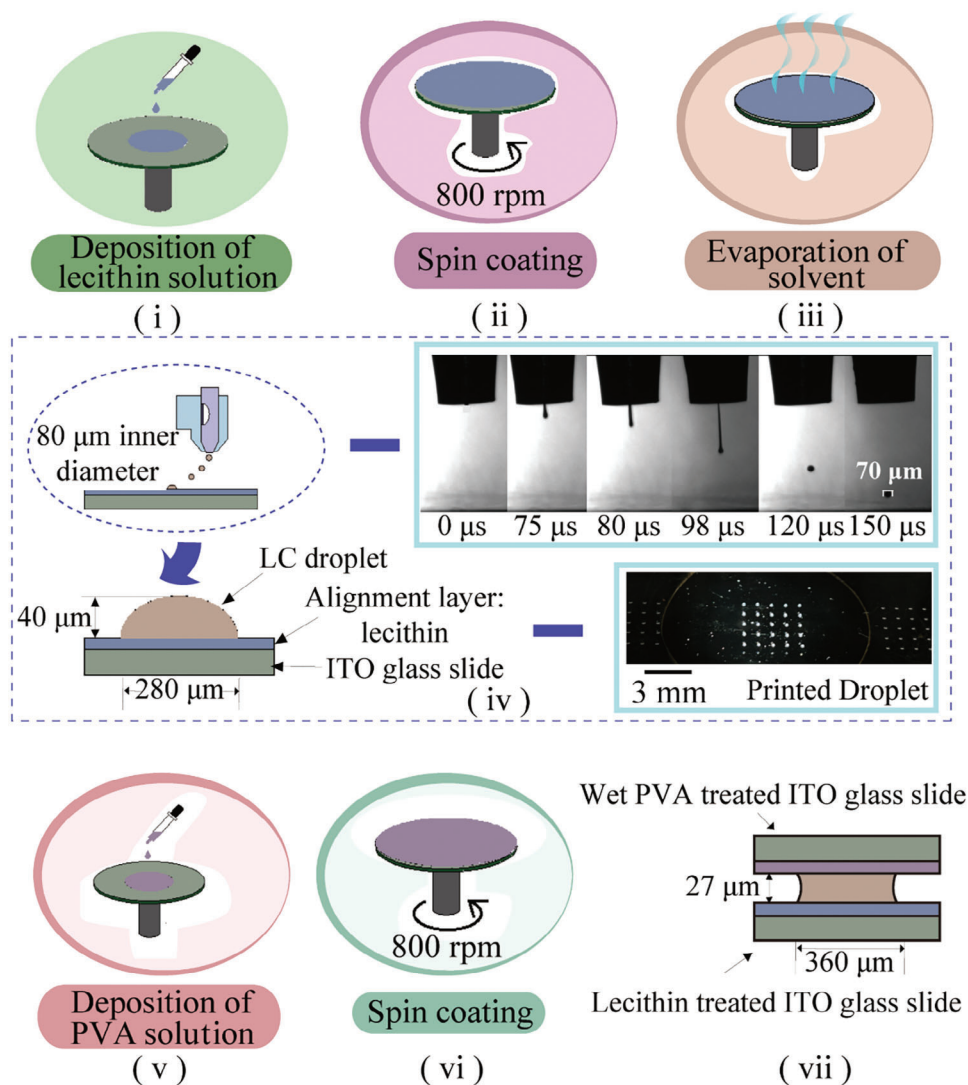


Figure 1. Fabrication process for the inkjet-printed LC optical vortex beam generators. i–iii) Deposition and spin-coating of the lecithin solution for the homeotropic alignment layer. iv) Process for printing LC droplets (and arrays thereof) onto the lecithin treated substrate. This includes an illustration of the side profile of a printed droplet, shadowgraphy images showing the deposition of the LC, and a photograph of a 5 × 5 array of printed LC droplets. The inner diameter of the printhead used in this work was 80 μm. 32 droplets were printed onto the same location on the substrate resulting in a final footprint diameter of the droplet of 280 μm. The height of the droplet was determined from shadowgraphy images to be 40 μm. v,vi) Deposition and spin-coating of the wet PVA solution onto the top substrate to promote a radial alignment of the LC direct. vii) Illustration of the inkjet-printed LC vortex beam generator device with a diameter of 360 μm and a height of 27 μm. The nematic LC in this case is the eutectic mixture, E7.

where a $\pi/2$ shift was observed in the fast axis distribution. This shift arises from the algorithm employed for the calculation of the MM, as well as the subsequent decomposition process for the retardance and the fast axis distribution results. During data processing, the algorithm was designed to induce a flip when the retardance exceeded π , concurrently causing the fast axis to undergo a $\pi/2$ shift. This phenomenon was not isolated to the case presented but also manifests in the outer ring of the retardance in Figure 2b and the fast axis distribution in both Figure 2b,c. The circular pattern in the central region of the field-off condition, as seen in both the retardance and fast axis orientation diagrams, can be attributed to a non-uniform director alignment in this area. This central region was minimized with the

application of an electric field (c.f. Figure 2b,c). For our droplets, the switching relaxation time is around 0.4 s. The reason is that the response time of nematic LC devices is generally controlled by the length scale of the structure formed, together with the elastic and viscous properties of the material. In our droplet devices, the key length scale is the thickness of the LC droplet layer in the device. Therefore, the switching time of our devices is very similar to that of a hybrid aligned nematic layer of 27 μm thickness. With the nematic LC, E7, such a layer has a relaxation time of ≈ 0.4 s.

To complement the results from experiments, simulations were conducted based upon continuum theory. The theory takes into account the elastic free-energy, which describes the

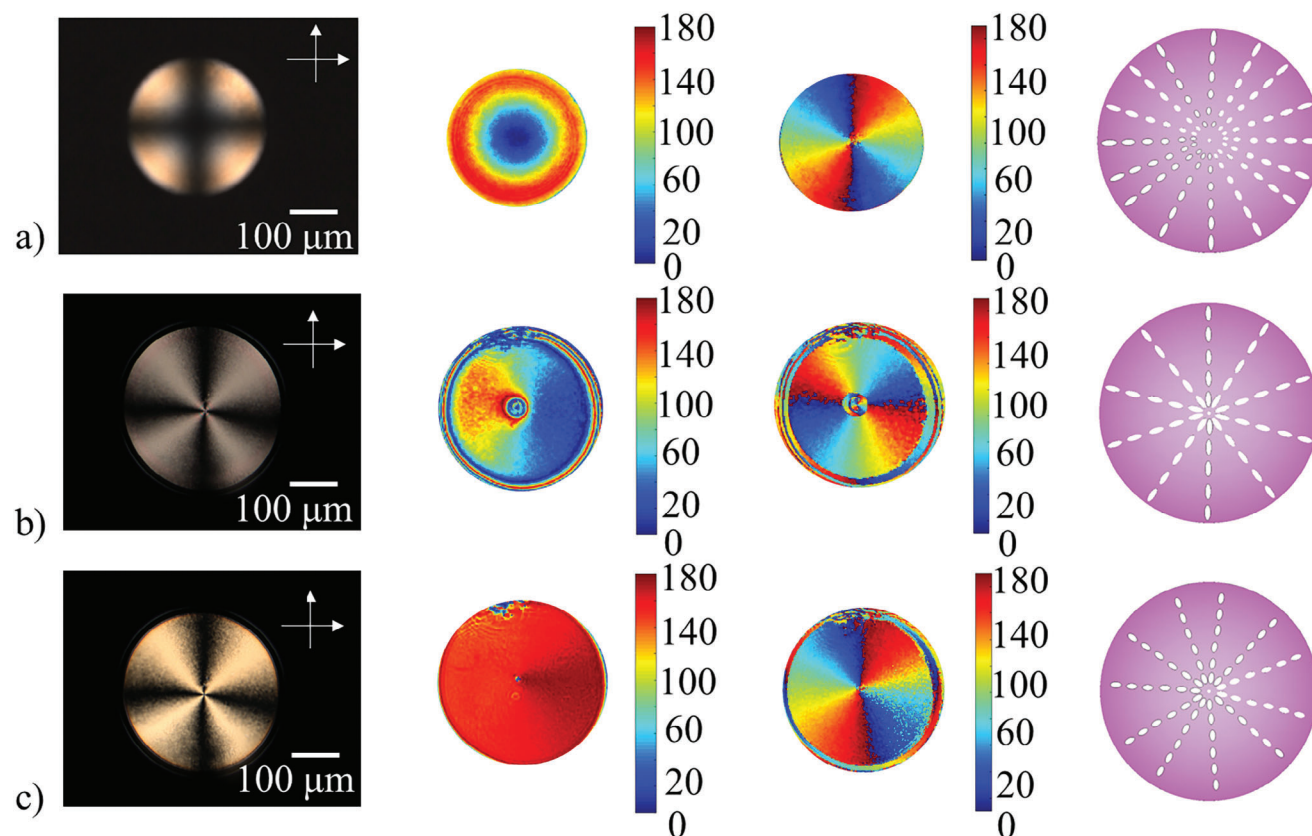


Figure 2. A comparison of the optical properties of a printed LC vortex beam generator. a) Nematic LC droplet printed onto a lecithin-treated glass substrate. b) The printed LC vortex beam generator (i.e., printed LC droplet between a PVA-coated glass substrate and the lecithin-coated glass substrate) with no applied electric field. c) The printed LC vortex beam generator with an applied electric field of $E = 0.17 \text{ V } \mu\text{m}^{-1}$ (square wave, frequency = 1 kHz). The images in each row are as follows: the first image in this sequence is a polarizing optical microscope image (white single-headed arrows denote the orientations of the polarizer and analyzer) while the second image shows the corresponding retardance extracted from Mueller Matrix (MM) polarimetry. The third image shows the fast axis distribution (also obtained from MM polarimetry) and the fourth image illustrates schematically the corresponding internal director distribution. The nematic LC was the mixture E7, and the measurements were carried out at a temperature of 25 °C. The thickness of the LC layer in (b,c) was 27 μm .

correlation between the energy and the distortion that results from any external influences. The free-energy per unit volume (f_v) for an achiral nematic LC can be written as,

$$f_v = \frac{1}{2} K_1 [\nabla \cdot \mathbf{n}]^2 + \frac{1}{2} K_2 [\mathbf{n} \cdot (\nabla \times \mathbf{n})]^2 + \frac{1}{2} K_3 |\mathbf{n} \times (\nabla \times \mathbf{n})|^2 \quad (1)$$

where \mathbf{n} represents the director while K_1 , K_2 , and K_3 are constants representing the splay, twist, and bend distortions of the director, respectively. These three constants describe the “rigidity” of the LC to director distortion. Simulations were carried out including parameters such as the diameter and height of the droplet vortex beam generator as well as the physical parameters of the nematic LC mixture, E7. As discussed, the optical properties of these devices are intrinsically influenced by the distribution of the LC director.

Figure 3 provides an illustration of the director distributions in a cross-section of the droplet/droplet device, alongside their respective simulation results, including the retardance and the orientation of the fast axis from the central point of the droplet device to the peripheral ring. **Figure 3a** presents the results for

an LC droplet printed onto the lecithin-treated glass substrate before the assembly of the vortex beam generator device (step iv) in **Figure 1**. Subsequently, **Figure 3b** displays the results from simulations for the vortex beam generator device in the absence of any applied electric field, while **Figure 3c** shows the behavior when an electric field was applied that was of the precise amplitude required for the director distribution to generate a vortex beam output.

Each row in the figure presents a distinct set of sub-figures corresponding to different states. The first sub-figure in each row (far left) schematically illustrates the director distribution for the respective state. This is followed by a second sub-figure that depicts a 2D simulation of the LC director profile, extending from the central point of the droplet to its outer ring. Subsequently, the third sub-figure shows the simulation results for the retardance, derived from the simulated director distribution diagram, thereby shedding light on the link between the director distribution and the resultant retardance. The fourth sub-figure (far right) in each row presents the corresponding simulated fast axis distribution, which complements the preceding retardance simulation.

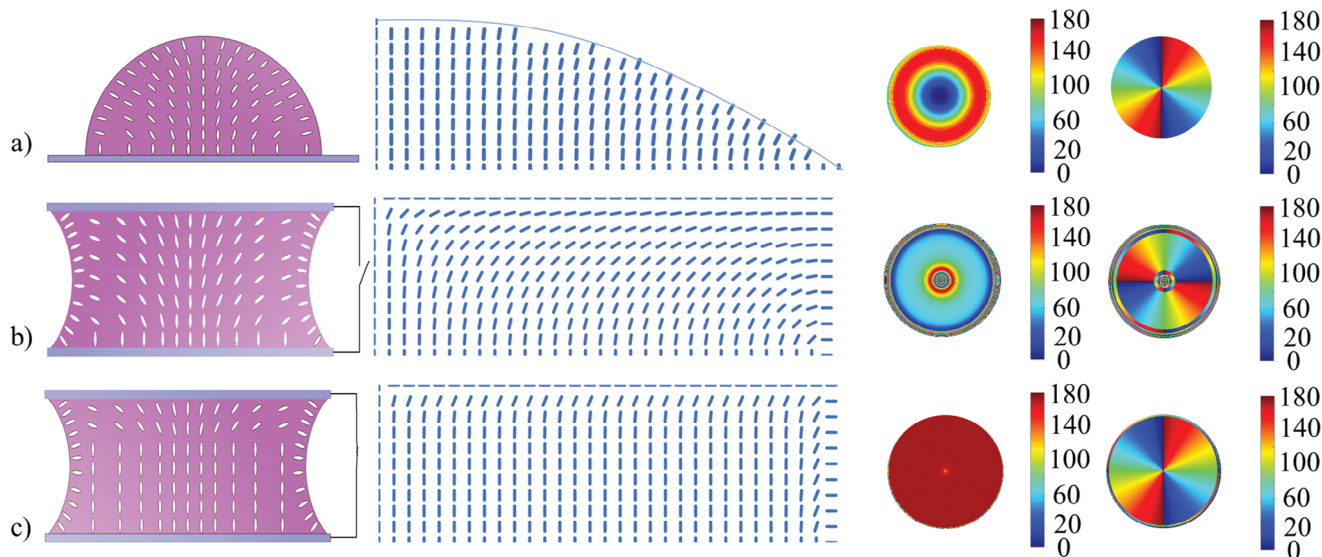


Figure 3. Simulations of the director distribution within the vortex beam generator. a) Results for a single LC droplet printed onto a lecithin-treated glass substrate. b) Printed droplet device where no electric field is applied. c) Printed droplet device under conditions of appropriate electric field amplitude. For each depicted device, the sequence of images begins on the far left with a side view illustrating the director distribution, then the respective 2D director simulation results (ranging from the center to the outermost edge of the printed droplets), followed by the simulated retardance (3rd column) and fast axis profiles (4th column).

Using the average tilt angle of the LC director to represent the director distribution from the center point to the outer boundary reveals that different devices display distinct average tilt angles. The retardance was calculated via the following equation:

$$R = 2\pi \int \left(\frac{n_e \cdot n_o}{\sqrt{n_o^2 \cdot \cos^2 \theta + n_e^2 \cdot \sin^2 \theta}} - n_o \right) \cdot \frac{dz}{\lambda} \quad (2)$$

In the equation, d is the physical thickness of the droplet device; λ is the wavelength of the incident Gaussian beam; θ is the tilt angle of the LC director; n_e is the extraordinary refractive index; and n_o is the ordinary refractive index of the nematic LC. Therefore, the retardance is decided not only by the tilt angle of the LC director, but also by the thickness of the LC layer in the droplet device.

For the single LC droplet printed onto the lecithin glass substrate, the average tilt angle was observed to change continuously. When the retardance was calculated based on this LC director distribution, it was also found to vary, which does not meet the requirements for vortex light generation. For the printed droplet device without the application of an external electric field, as we move from the center of the droplet the average LC tilt angle initially decreases, then stabilizes at a certain value before dropping to zero at the droplet edge. In contrast, when a suitable amplitude of electric field was applied, the trend in terms of changes in the average LC tilt angle remains the same, but the overall maintained value remained relatively high. This resulted in a different retardance profile. Nonetheless, as the LC director only tilts within the vertical plane, the direction of the director's minor axis remains in the annular direction. One thing to note is that in the process of mapping retardance, the values were constrained

to a range of 0 to 180°. This was done in order to be consistent with the images of retardance extracted from the MM polarimetry, which cannot measure the total accumulated retardance. The total calculated accumulated retardance values, derived from the simulations of the LC director profile, for the LC droplet under the application of an electric field are presented in Figure S1 (Supporting Information).

An analysis of the retardance and fast axis distributions, derived from the simulated director profile, indicates a strong correlation between the simulation results presented in Figure 3 and the experimental data obtained using a MM polarimeter as depicted in Figure 2, validating the efficacy of the modelling approach. There is evidently greater uniformity exhibited in the simulation results, particularly in terms of retardance, whereas it can be seen that there is some non-uniformity in the retardance in the experimental results. This discrepancy primarily stems from imperfections in the alignment layer leading to non-ideal LC director alignment. When an electric field was applied, the LC director reoriented under the influence of the electric field, resulting in relatively uniform retardance, and thus very good agreement between the results from simulations and experiments.

To elucidate the processes involved in vortex beam formation, a simulation protocol was executed. The procedure is graphically presented in Figure S2 (Supporting Information). The simulation commences with the introduction of a Gaussian beam as the input light, which can be manipulated in terms of dimensions, peak intensity, and spatial positioning, thereby allowing the investigation of the influence these parameters have on the resulting output beam. The Gaussian beam subsequently passes through a spatially structured phase distribution, which is controlled by the director distribution identified earlier. This plays a key role in forming the input light into a vortex beam, and its structure impacts the characteristics of the resulting

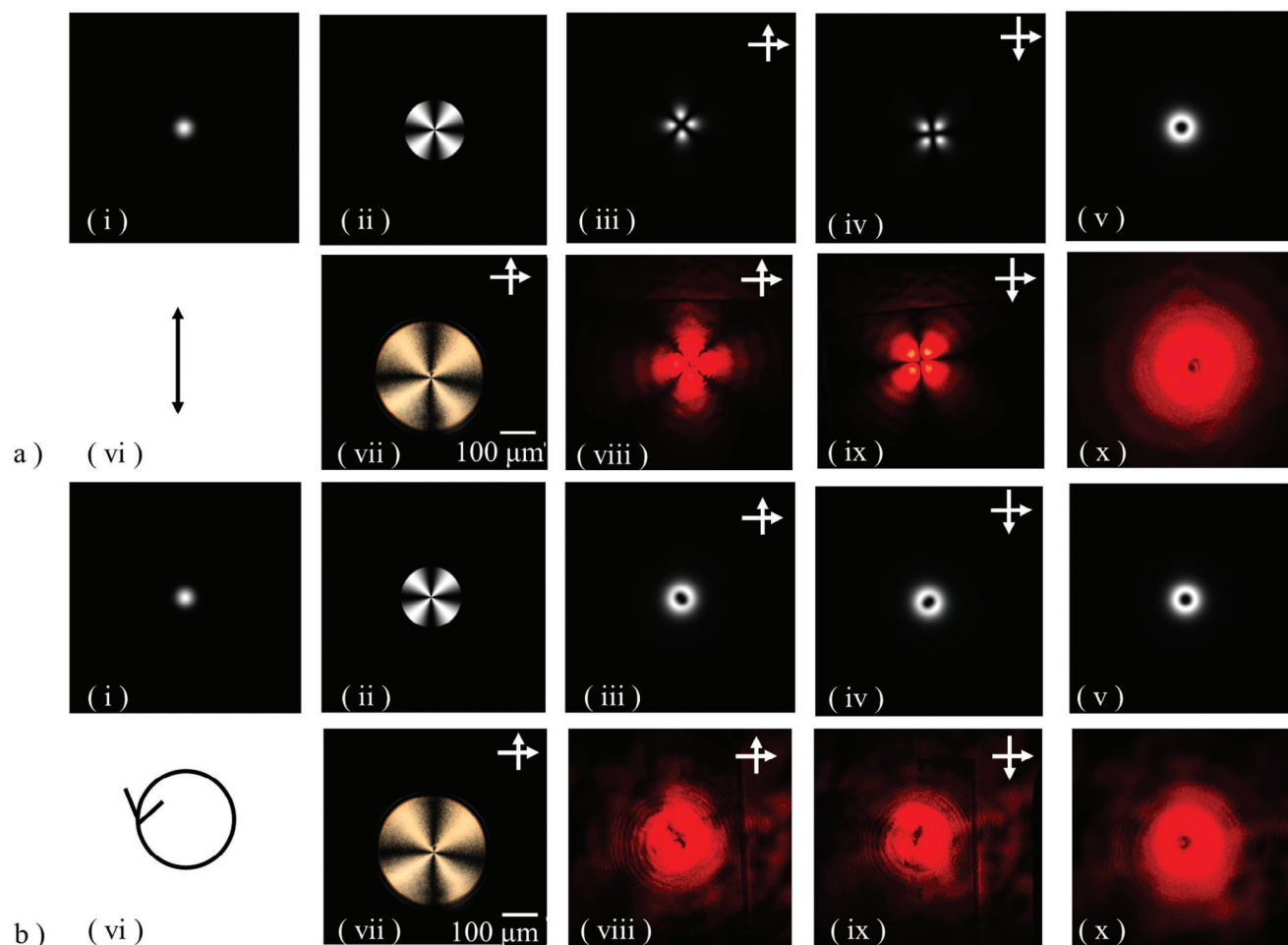


Figure 4. Generation of the far-field vector beam (with linearly polarized input light) a) and the vortex beam (with circularly polarized input light) b) for a printed LC droplet device. For both a,b) the first row presents simulation results: (i) is the input Gaussian beam, while (ii) portrays the intensity of light transmission following its traversal through the printed LC device. (iii) depicts the distribution of the far-field intensity observed when a polarizer was placed after the device and before the far-field observation plane and (iv) is the same but with the polarizer rotated by an angle of 90° . (v) shows the cumulative far-field intensity. The second row presents the corresponding experimental results: (vi) indicates that the input light is either linearly polarized or circularly polarized, and (vii) shows the printed LC droplet device on a POM with crossed polarizers and an electric field of $E = 0.17 \text{ V } \mu\text{m}^{-1}$. (viii,ix) Display the far-field images when the polarizer was placed between the device and the far-field were set at angles of 0° and 90° , respectively. Lastly, (x) demonstrates the far-field pattern in the absence of a polarizer.

vortex beam. Simulations conducted by considering the printed LC droplet as a waveplate without accounting for the distribution of the LC director are presented in Figure S3 (Supporting Information).

Following the determination of the phase distribution using Jones matrices, the far-field intensity pattern was then determined using Fourier transform techniques. To verify the results from simulations, the far-field intensity profiles were determined experimentally using an arrangement as depicted in the schematic presented in Figure S4 (Supporting Information). Examination of both the lecithin-treated glass substrate with a single printed LC droplet and the vortex beam generator, in both the non-electric field and non-optimal electric field conditions, revealed an absence of a vortex beam in the far-field. However, with the application of an electric field of the appropriate amplitude a vortex beam, bearing the characteristic “doughnut-shaped” intensity profile, appeared in the far-field.

Results from the simulations and experiments are shown in Figure 4 for different polarizations of the input light. It is shown that both vector and vortex beams can be generated depending on the characteristics of the incident light. For example, with linearly polarized incident light, a vector beam was created, as shown in Figure 4a. Conversely, when the incident light was circularly polarized, it resulted in the formation of a vortex beam, demonstrated in Figure 4b. The upper row of Figure 4a presents the results from the simulation process. Here, the incident light was a linearly polarized Gaussian beam. After undergoing Fourier transformation, the resultant far-field vector beam is depicted in Figure 4a-v. This beam can be decomposed into two mutually perpendicular directions, as exhibited in Figure 4a-iii,iv. Analogous experimental results were obtained as shown in the second row of Figure 4a. The experiments demonstrate that when a laser with a wavelength of 633 nm was transmitted through the device, the result was the formation of a vector beam in the

far-field (Figure 4a-x), in accordance with the results from simulations (Figure 4a-v). The corresponding far-field images, as seen in Figure 4a-viii,ix, were obtained by positioning a polarizer at a relative orientation of 90° between the device and the far-field, which are in good agreement with Figure 4a-iii,iv. These findings in combination exemplify the generation process of the vector beam.

In contrast, when the input light was circularly polarized, a vortex beam appeared in the far-field. Utilizing the same methodology as before, the two decomposed far-field intensities in mutually perpendicular directions were determined from simulations to be as shown in Figure 4b-iii,iv. The simulations show clearly that when these two far-field intensity profiles are combined the complete far-field intensity (presented in Figure 4b-v) show the formation of a vortex beam. Experiments yielded similar results: by introducing a polarizer between the device and the far-field and rotating it by 90° enabled to two components of the far-field to be decoupled (Figure 4b-viii,ix), in accordance with the simulations. Without the polarizer, the vortex beam can be seen in its entirety (shown in Figure 4b-x). These findings demonstrate the generation process of the vortex beam. In this circumstance, if the electric field amplitude is altered the resulting LC director distribution changes and a vortex beam cannot be generated, as shown in Figure S5 (Supporting Information). Consequently, the research presented herein demonstrates the proficiency of the inkjet printed LC droplet vortex beam generator in effectively producing both vector and vortex beams.

In summary, our device offers an alternative and straightforward method for fabricating switchable vortex beam generators. Details comparing different vortex beam generators are available in Table S1 (Supporting Information). With drop-on-demand inkjet printing technology, the device we have reported here features a customizable design with a low thickness. This compact form provides the possibility for the generator to be integrated into various complex optical systems.

3. Conclusion

This paper demonstrates an efficient and practical methodology for the generation of vortex beams utilizing a device that contains a sub-millimeter diameter liquid crystal (LC) droplet that has been fabricated using drop-on-demand inkjet printing technology. The representative device, possessing a footprint diameter of 360 µm and an LC layer thickness of 27 µm, is shown to be capable of generating both vector and vortex beams upon the application of an electric field with an amplitude of $E = 0.17 \text{ V } \mu\text{m}^{-1}$. The type of beam that is formed is contingent upon the polarization state of the incident light. The fabrication process of this device is highly versatile, with the added advantage of enabling customization in terms of the dimensions of the device and the ability to create arrays of vortex beam generators of different configurations. Furthermore, the technique can be readily translated to mass production for applications that potentially demand high device volumes such as optical communications.

4. Experimental Section

Materials: A nematic LC, E7 from Synthon Chemicals Ltd with ordinary refractive index, $n_o = 1.52$, and extraordinary refractive index, $n_e = 1.74$, at

a wavelength of 633 nm and a temperature of 20 °C, was the primary material used in this vortex beam generator. Lecithin from Merck was diluted to 1% weight solution in an isopropanol (IPA) solvent from Merck, which was used to align the LC director homeotropically. Polyvinyl alcohol (PVA) was purchased from Merck and dissolved in deionized water (DI water) at a temperature of 100 °C with magnetic stirring for 6 hours to obtain a 10% PVA solution.

Fabrication Process: The whole vortex beam generator fabrication process is shown in Figure 1. Indium tin oxide (ITO) coated glass slides (Ossila) were cleaned with acetone (VWR Chemicals), IPA and DI water successively. Lecithin solution was then spin-coated on the surface of the clean ITO-coated glass slide at 800 rpm for 2 min and then dried on a hot plate for 1 min. The LC was printed on the lecithin treated slide using a Jetlab-II printing system from MicroFab Technologies Inc. This printing system is highly automated with a three-axis translation platform used to adjust the printing position and printing height by allowing the nozzle to move freely along three orthogonal axes. A camera was placed at the same level as the print head, which enabled observation of the shape and quality of the printed droplets.

For the printing process, an 80 µm inner diameter nozzle (MicroFab MJ-AT-01-80) was used which could print LC droplets with an in-flight diameter of 70 µm and 95 µm footprint diameter when deposited on the substrate. The physical properties of the printed LC ink, such as the viscosity and the surface tension, have a notable influence on the printing process. For nematic LCs, printing was investigated with a 50 µm inner diameter nozzle, which is smaller than the nozzle that was used to generate the results presented in this paper. However, the printing process using such a nozzle was found to be somewhat unstable, due in particular to the combination of viscosity and surface tension of the nematic LC. The 80 µm inner diameter nozzle was therefore chosen to realize a stable and uniform printing process. The clearing temperature of the nematic LC used in this study (E7) was 58 °C. Therefore, if the temperature of the nozzle was heated to above 58 °C, the LC ink will be in the isotropic phase which is substantially less viscous than that at room temperature.

Using the printing conditions described above, and by printing 32 times at the same location, droplets with a footprint diameter of 280 µm were obtained. Two spacers were attached on the sides of the slide. Another ITO slide was then spin-coated with 10% PVA solution at 800 rpm for 30s and the treated slide was directly placed on the top of the printed droplets to make sure the PVA solution was in a wet state when attached to the other side. Pressure was applied to the device and an ultraviolet (UV) curable glue was coated onto the edge of the device. The whole device was then placed in a UVP Crosslinker (analytikjena) for 20 min. After being sandwiched by the two ITO-coated glass slides, the thickness of the LC layer between the glass substrates was 27 µm while the diameter of the printed LC droplet was found to be 360 µm. This particular diameter was chosen based on the findings that the diameter of the droplet can influence the operational performance of the printed LC droplet device. The working principle for the vortex beam generator is based on the area of radial orientation of the LC director's alignment. Therefore, the functional area is the area between the center point of the droplet and the outer area where the retardance is around π . As illustrated in Figure S6 (Supporting Information), for a very small droplet the director distortion extends over a large proportion of the area and the functional area is then too small to generate a vortex beam. Alternatively, for rather large droplets, the flow of the LC at the wet PVA surface during device assembly means that the surface anchoring may not be able to form a radial alignment over the entire droplet area. Following preliminary experiments, the 360 µm droplet device was then chosen to generate the vortex beam generator as described in this paper.

In this fabrication process, the LC director aligns in a specific way. When the LC is first printed onto the lecithin treated substrate, it provides vertical alignment of the LC director at the substrate interface. Because of the surface tension, the LC director tends to align perpendicular to the interface of LC and the air as shown in Figure 3a). When the wet PVA coated substrate is attached on the top of the printed droplet, due to the pre tilt of the LC director (caused by the surface tension), the LC director tends to align parallel to the wet PVA coated substrate along the pre tilt direction. This is

because, unlike rubbed PVA, the wet PVA provides planar alignment with no prior preferred direction. This provides the LC director configuration as shown in Figure 3b) which following voltage application becomes the director profile shown in Figure 3c).

Polarizing Optical Microscopy: The printed droplets and fabricated device were observed on an Olympus BX51 polarizing optical microscope. In order to apply an electric field to the printed droplet device, a function generator (Multicomp PRO) was employed, and an oscilloscope (Tektronix) was used to display the voltage waveform applied to the device in real-time.

Mueller Matrix Polarimetry: Mueller matrix (MM) polarimetry was employed to assess the optical attributes of the devices, including the retardance and fast axis orientation. The MM polarimeter involved the use of a gradient-index (GRIN) lens, a polarization state generator (PSG), and a polarization state analyzer (PSA). Both the PSG and the PSA consisted of a polarizer and a motor-controlled quarter-wave plates. A set of 30 images were captured based on varying combinations of the PSG and PSA states. From these images, the MM of the printed droplet and printed droplet devices were computed, subsequently enabling the decomposition of the retardance and fast axis distribution.

Far-Field Experiment: The experimental setup used to record the images in the far-field is shown in Figure S4 (Supporting Information). The experiment configuration incorporated a helium-neon laser (JDS Uniphase, 1122P) with $\lambda = 633$ nm as the light source, a neutral density (ND) filter (Thorlabs) was used to lower the intensity of the laser beam and a lens (Thorlabs) with 200 mm focal length was used to shrink the incident laser beam radius to a size smaller than the diameter of the LC droplet. To convert linearly polarized light into circularly polarized light, a quarter wave plate (Thorlabs) designed for operation at 633 nm was used. The voltage applied to the device was gradually ramped up in 0.1 V_{pp} increments until it reached an electric field of $E = 0.17$ V μm^{-1} , at which point a vortex beam could be seen in the far-field.

Simulations: The first phase of the simulation involved calculating the distribution of the LC director from which the retardance and fast axis distribution were derived. In the next phase of the simulations, a Gaussian input beam was defined and the propagation of this beam through the device under study was then simulated using Jones matrices. Finally, the total output field and the corresponding far-field intensity patterns were then computed.

Supporting Information

Supporting Information is available from the Wiley Online Library or from the author.

Acknowledgements

A.A.C.-P. was supported by The Royal Society through a University Research Fellowship (URF\R\180016) and the John Fell Fund, Oxford University Press, via a Pump-Priming grant (0005176). The authors gratefully acknowledge the John Fell Fund, Oxford University Press, via a Pump-Priming grant (0005519). C. H. acknowledges financial support from St John's College (Oxford) for a Junior Research Fellowship.

Conflict of Interest

The authors declare no conflict of interest.

Data Availability Statement

The data that support the findings of this study are available from the corresponding author upon reasonable request.

Keywords

inkjet printing, liquid crystals, optical vector fields, vortex beams

Received: February 17, 2024

Revised: May 3, 2024

Published online: June 17, 2024

- [1] Y. Liang, Y. Cai, Z. Wang, M. Lei, Z. Cao, Y. Wang, M. Li, S. Yan, P. R. Bianco, B. Yao, *Appl. Opt.* **2018**, 57, 3618.
- [2] A. Yakimenko, Y. M. Bidasyuk, O. Prikhodko, S. Vilchinskii, E. Ostrovskaya, Y. S. Kivshar, *Phys. Rev. A* **2013**, 88, 043637.
- [3] V. Kotlyar, A. Kovalev, A. Porfirev, *J. Appl. Phys.* **2016**, 120, 023101.
- [4] K.-i. Yuyama, H. Kawaguchi, R. Wei, T. Omatsu, *ACS Photonics* **2023**, 10, 4045.
- [5] Z. Wang, N. Zhang, X.-C. Yuan, *Opt. Express* **2011**, 19, 482.
- [6] W. Shao, S. Huang, X. Liu, M. Chen, *Opt. Commun.* **2018**, 427, 545.
- [7] R. Gauthier, *J. Phys.: Conf. Ser.* **2019**, 1251, 012016.
- [8] G. S. Agarwal, J. Banerji, *J. Phys. A: Math. Gen.* **2006**, 39, 11503.
- [9] P. Miao, Z. Zhang, J. Sun, W. Walasik, S. Longhi, N. M. Litchinitser, L. Feng, *Science* **2016**, 353, 464.
- [10] A. Mamaev, M. Saffman, A. Zozulya, *Phys. Rev. Lett.* **1996**, 77, 4544.
- [11] H. Singh, *Opt. Appl.* **2017**, 47, 4.
- [12] D. Mihalache, *Rom. Rep. Phys.* **2007**, 59, 515.
- [13] F. Takahashi, K. Miyamoto, H. Hidai, K. Yamane, R. Morita, T. Omatsu, *Sci. Rep.* **2016**, 6, 21738.
- [14] S. Wei, T. Lei, L. Du, C. Zhang, H. Chen, Y. Yang, S. Zhu, X.-C. Yuan, *Opt. Express* **2015**, 23, 30143.
- [15] J. Park, P. Eames, D. Engebretson, J. Berezovsky, P. Crowell, *Phys. Rev. B* **2003**, 67, 020403.
- [16] C. Zhang, C. Min, L. Du, X.-C. Yuan, *Appl. Phys. Lett.* **2016**, 108, 201601.
- [17] A. Popiołek-Masajada, J. Masajada, M. Szatkowski, *Opt. Lasers Eng.* **2018**, 105, 201.
- [18] Y. Shen, X. Wang, Z. Xie, C. Min, X. Fu, Q. Liu, M. Gong, X. Yuan, *Light: Sci. Appl.* **2019**, 8, 90.
- [19] X. Zhuang, *Science* **2004**, 305, 188.
- [20] S. Syubaev, A. Zhizhchenko, A. Kuchmizhak, A. Porfirev, E. Pustovalov, O. Vitrik, Y. Kulchin, S. Khonina, S. Kudryashov, *Opt. Express* **2017**, 25, 10214.
- [21] W. Lee, X.-C. Yuan, W. Cheong, *Opt. Lett.* **2004**, 29, 1796.
- [22] S. N. Khonina, A. V. Ustinov, V. I. Logachev, A. P. Porfirev, *Phys. Rev. A* **2020**, 101, 043829.
- [23] H. Wei, A. K. Amrithanath, S. Krishnaswamy, *IEEE Photonics Technol. Lett.* **2019**, 31, 599.
- [24] Y. Yang, X. Ye, L. Niu, K. Wang, Z. Yang, J. Liu, *Opt. Express* **2020**, 28, 1417.
- [25] C. Liu, X. Wei, L. Niu, K. Wang, Z. Yang, J. Liu, *Opt. Express* **2016**, 24, 12534.
- [26] A. V. Carpentier, H. Michinel, J. R. Salgueiro, D. Olivieri, *Am. J. Phys.* **2008**, 76, 916.
- [27] B. Terhalle, A. Langner, B. Päivänranta, V. A. Guzenko, C. David, Y. Ekinci, *Opt. Lett.* **2011**, 36, 4143.
- [28] S. Li, Z. Wang, *Appl. Phys. Lett.* **2013**, 103, 141110.
- [29] R. K. Tyson, M. Scipioni, J. Viegas, *Appl. Opt.* **2008**, 47, 6300.
- [30] M. Scipioni, R. K. Tyson, J. Viegas, *Appl. Opt.* **2008**, 47, 5098.
- [31] M. Beresna, M. Gecevičius, P. G. Kazansky, T. Gertus, *Appl. Phys. Lett.* **2011**, 98, 201101.
- [32] J. Lu, L. Meng, F. Shi, X. Liu, Z. Luo, P. Yan, L. Huang, F. Pang, T. Wang, X. Zeng, *Opt. Lett.* **2018**, 43, 5841.
- [33] R. Chen, J. Wang, X. Zhang, J. Yao, H. Ming, A. Wang, *Opto-Electron. Adv.* **2018**, 1, 180003.

- [34] D. P. Ghai, *Appl. Opt.* **2011**, 50, 1374.
- [35] Y. Izdebskaya, V. Shvedov, A. Volyar, *Opt. Lett.* **2005**, 30, 2472.
- [36] F. Yue, D. Wen, J. Xin, B. D. Gerardot, J. Li, X. Chen, *ACS Photonics*. **2016**, 3, 1558.
- [37] B. Liu, Y. He, S. W. Wong, Y. Li, *Adv. Opt. Mater.* **2021**, 9, 2001689.
- [38] S. Tang, X. Li, W. Pan, J. Zhou, T. Jiang, F. Ding, *Opt. Express*. **2019**, 27, 4281.
- [39] E. Melnikova, D. Gorbach, S. Slussarenko sr, A. Muravsky, A. Tolstik, S. Slussarenko jr, *Opt. Commun.* **2022**, 522, 128661.
- [40] R. Barboza, U. Bortolozzo, M. Clerc, S. Residori, E. Vidal-Henriquez, *Adv. Opt. Photonics*. **2015**, 7, 635.
- [41] E. Brasselet, N. Murazawa, H. Misawa, S. Juodkazis, *Phys. Rev. Lett.* **2009**, 103, 103903.
- [42] R. Barboza, T. Sauma, U. Bortolozzo, G. Assanto, M. Clerc, S. Residori, *New J. Phys.* **2013**, 15, 013028.
- [43] R. Barboza, U. Bortolozzo, M. Clerc, S. Residori, E. Vidal-Henriquez, *Philos. Trans. R. Soc., A*. **2014**, 372, 20140019.
- [44] D. Lee, H. Lee, L. Migara, K. Kwak, V. P. Panov, J. K. Song, *Adv. Opt. Mater.* **2021**, 9, 2001604.
- [45] T. Boland, T. Xu, B. Damon, X. Cui, *Biotechnol. J.: Healthcare Nutr. Technol.* **2006**, 1, 910.
- [46] S. Azizi Macheuposhti, S. Movahed, R. J. Narayan, *Biophys. Rev.* **2020**, 1, 011301.
- [47] N. Scoutaris, S. Ross, D. Douroumis, *Pharm. Res.* **2016**, 33, 1799.
- [48] A. Sajedi-Moghaddam, E. Rahmanian, N. Naseri, *ACS Appl. Mater. Interfaces*. **2020**, 12, 34487.
- [49] V. Beedasy, P. J. Smith, *Materials*. **2020**, 13, 704.
- [50] M. Gao, L. Li, Y. Song, *J. Mater. Chem. C*. **2017**, 5, 2971.
- [51] Z. Yin, Y. Huang, N. Bu, X. Wang, Y. Xiong, *Chin. Sci. Bull.* **2010**, 55, 3383.
- [52] S. Kim, A. Traille, H. Lee, H. Aubert, K. Yoshihiro, A. Georgiadis, A. Collado, M. M. Tentzeris, in *Proc. of the 43rd European Microwave Conf.*, **2013**, pp. 866–869.
- [53] H. Jiang, W. Yu, J. F. Waimin, N. Glassmaker, N. Raghunathan, X. Jiang, B. Ziaie, R. Rahimi, in *2019 IEEE SENSORS*, IEEE, Montreal, QC, Canada **2019**, pp. 1–4.
- [54] Q. Zheng, J. Lu, H. Chen, L. Huang, J. Cai, Z. Xu, *Anal. Biochem.* **2011**, 410, 171.
- [55] N. Scoutaris, F. Chai, B. Maurel, J. Sobocinski, M. Zhao, J. G. Moffat, D. Q. Craig, B. Martel, N. Blanchemain, D. Douroumis, *Mol. Pharm.* **2016**, 13, 125.
- [56] H. He, R. Liao, N. Zeng, P. Li, Z. Chen, X. Liu, H. Ma, J. *Lightwave Technol.* **2019**, 37, 2534.